The importance of fracture toughness evaluation for additively manufactured metals

Moses J. Paul [a] [b], Jamie J. Kruzic [a], Upadrasta Ramamurty [b] [c] [1], Bernd Gludovatz [a]

[a]

School of Mechanical and Manufacturing Engineering, University of New South Wales (UNSW Sydney), Sydney, NSW 2052, Australia

[b]

School of Mechanical and Aerospace Engineering, Nanyang Technological University, Singapore 639798, Republic of Singapore

[c]

Institute of Materials Research and Engineering (IMRE), Agency for Science, Technology and Research (A*STAR), Singapore 138634, Republic of Singapore

Abstract

Yield strength and fracture toughness are key properties of structural materials used by designers for engineering applications, whereas secondary properties like ductility are not generally used in quantitative design calculations. However, since ductility is usually measured along with strength in the same tensile test, it is often used as an indication of the fracture toughness even though these properties are usually not directly proportional. As a result, many researchers initially, and only, screen new materials and processing routes for good combinations of strength and ductility rather than evaluating fracture toughness independently. This can result in poorly informed decisions being made early in the development stages for structural applications where materials with combinations of high strength and good fracture toughness are required. In this article, we evaluate the correlation between fracture toughness and ductility of Al-, Fe-, and Ti-based alloys that were processed using conventional methods as well as by additive manufacturing (AM) routes. We highlight that the correlation between fracture toughness and ductility is very weak, which in the case of AM materials is attributed to their often-metastable microstructures, their layer-by-layer mesostructures, and their anisotropic failure characteristics that lead to pronounced variability in the fracture toughness data for materials with similar ductility. Our findings suggest that an independent assessment of fracture toughness alongside the tensile properties (strength and ductility) is required to correctly optimize the AM processing of structural materials and provide engineers with the properties required for the design of parts and components for structural and safety-critical applications.

Graphical abstract

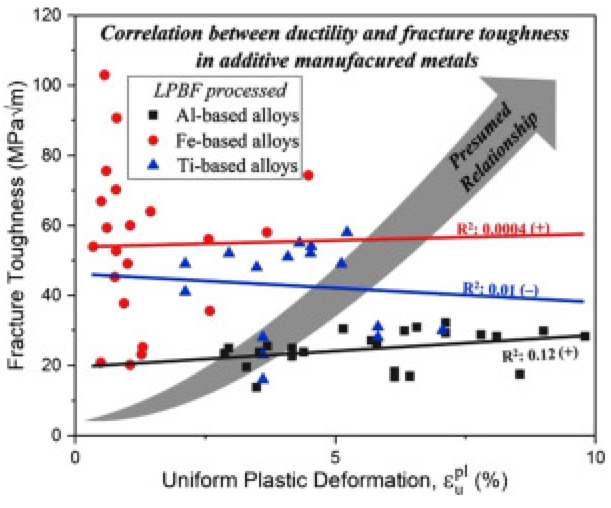

Keywords
Metals and alloys
Additive manufacturing
Micro and mesostructure
Ductility
Fracture toughness

1. Introduction

Various mechanical properties are evaluated and considered (often in combination) during alloy development as well as the material selection process for structural applications. The most commonly evaluated properties include Young's modulus (E), yield strength (σ_y), ultimate tensile strength (σ_{UTS}), ductility in terms of failure strain (ε_f), and fracture toughness (K_{Ic}). Additional properties, such as fatigue strength and creep resistance, become important for specific application scenarios such as fluctuating loads or elevated temperatures, respectively. Needless to say, cost and availability, in addition to the mechanical and functional performance metrics, play vital roles in the material selection process. Most mechanical properties (except for E, which is not particularly sensitive to microstructure) can be manipulated by altering the chemical composition of the alloy and/or the processing methodology and conditions, all of which can result in microstructural changes. The objective of such strategies is often to design alloys and their microstructures for an optimum combination of properties.

During the evaluation of the mechanical performance of an alloy, σ_y is often the first parameter that is examined critically, followed by ductility. Fracture toughness[2] and ductility[3] are both considered to be inversely related to strength [[1], [2], [3]]. Therefore, they are often considered indicative of each other, whereby an increase in ductility for a given alloy is thought to suggest enhanced fracture toughness. Consequently, a vast number of studies focus on the strength-ductility combination, which is relatively easier to experimentally assess through a simple tensile test. However, while a correlation between ductility and fracture toughness can be found in some cases, a one-to-one correspondence between them has not been reported. In some specific instances, the connection between ductility and fracture toughness does not even exist [[4], [5], [6]]; prominent examples are metallic glasses which have negligible tensile ductility but can exhibit excellent K_{Ic} values well exceeding 100 MPa√m [7].

The breakdown in the correlation of ductility and fracture toughness can be understood by considering that while ductility and fracture toughness both depend on the extent to which an alloy accommodates plastic deformation, the micro-mechanisms are vastly different. In the context of fracture toughness, plastic deformation is highly constrained in a small volume of material in the plastic zone ahead of the crack tip where a triaxial state of stress often prevails. Other non-plasticity factors can also contribute to the toughness such as the crack path tortuosity and local mode-mixity. In contrast, ductility is governed by the relatively unconstrained plastic deformation across the entire gauge section of a specimen. It is particularly sensitive to the nature and extent of strain hardening, necking, and defects that are randomly distributed within the gauge volume.

Additive manufacturing (AM) represents a relatively recent advancement in material processing, and a large amount of research has focused on how to achieve desirable combinations of mechanical properties using AM. It has been shown that in the as-fabricated state, the strengths of alloys fabricated using various AM techniques such as laser or electron beam powder bed fusion (PBF-LB or PBF-EB) and directed energy deposition (DED) are often much higher than those of materials processed using conventional manufacturing routes (such as casting, forging, rolling, etc.) [[8], [9], [10]]. Enhanced strength arises from the rapid solidification conditions that are inherent to the aforementioned AM methodologies that give refined microstructural features with substantially higher dislocation densities and super-saturation of the solute content [[10], [11], [12]]. Such improved strength, however, is often accompanied by low ductility – depending on the alloy – which may be related to the trade-off between strength and ductility as well as defects that are unique to AM materials. Moreover, because strength and ductility can be measured at the same time, most published reports hitherto have focused only on the strength-ductility trade-off, with relatively little attention being given to fracture toughness.

A distinct feature of AM materials is their often-pronounced mesostructure that forms due to the line-by-line and layer-by-layer build strategy. The length scale of such mesostructures can range from tens to hundreds of micrometers. They can influence the fracture toughness of AM alloys by introducing pronounced crack path tortuosity that is unrelated to plastic deformation and thus uncorrelated to ductility [[13], [14], [15], [16], [17]]. For example, in an Al-12Si alloy that was fabricated using PBF-LB [18], a substantial increase in strength is accompanied by a marked loss in ductility (to almost zero for some processing conditions) compared to cast material while the measured fracture toughness is more than double that of cast Al-12Si. Thus, if researchers make early-stage decisions regarding how to optimize the PBF-LB process parameters based on only strength and ductility measurements, they might completely miss finding the optimal combinations of strength and fracture toughness that would be most useful to design engineers.

Given that ductility (i) is sensitive to the specimen geometry used to measure failure strains, (ii) is not a design parameter that is quantitatively used in the engineering of structural components (unlike E, σ_y, K_{Ic}, etc.), and (iii) is inconsequential for AM alloys from the standpoint of enabling secondary deformation processing (such as forging and rolling) since the primary purpose (and unique advantage) of AM is to produce near-net shaped parts, it is our view that screening materials and AM processing parameters based on ductility has limited practical value. Instead, we suggest that researchers developing processing-structure-mechanical property correlations for AM alloys should focus their efforts on evaluating – and enhancing – the fracture toughness since 1) it is a direct engineering design parameter and, more importantly, 2) it dictates the ability of AM alloys to tolerate defects (e.g., lack of fusion, gas porosity, etc.) that are often inherent to the various AM processes.

To support this viewpoint, in this paper we examine the correlations between ductility and fracture toughness for the most widely studied alloy systems used in AM, namely, Al-, Fe-, and Ti-based alloys. Our analysis emphasizes the importance of reporting the fracture toughness of AM materials, as sole reliance on comparisons of ductility during the optimization of mechanical properties may not provide a comprehensive understanding of a material's mechanical performance. This approach will allow for a more useful evaluation of the potential of AM materials in various structural applications, ensuring their performance and durability.

2. Data curation

The following procedures were adhered to when collecting data on tensile and fracture toughness properties from the literature in an objective manner for the purpose of this study. A key issue for AM alloys is batch to batch variation in the microstructures and mechanical properties of produced parts. Keeping this in mind, only data sets that report both tensile properties (σ_y and ε_f) and mode I fracture toughness (K_{Ic}) from the same research group on the same batch (either in the same publication or in successive publications where the authors refer to the properties reported earlier by themselves) were considered.

Tensile properties: First, the considered tensile stress-strain responses were examined closely to ensure that the reported σ_y matched the estimated values from the stress-strain curves; in all cases, the stress corresponding to the ~0.2% strain-offset value was taken. Ductility is a considerably more complex problem, particularly as many studies report ε_f as a measure of ductility. While this approach may be acceptable for materials that exhibit only limited necking across their plastic deformation regime (like some Ti-based alloys), most metals do show necking which effects the failure strain differently depending on the specimen dimensions and test methods used. Therefore, in this study ductility was defined two different ways to search for correlations with fracture toughness: i) as the total elongation to failure, ε_f – this is how ductility is reported in most published articles – and ii) the uniform plastic deformation strain, εupl, i.e., the difference between the strain corresponding to the yield and peak engineering stress (σ_y and σ_{UTS}), as illustrated in the schematic of Fig. A1. For the latter case of εupl, full stress strain curves were required, which were only available for the AM studies because for the conventional alloy studies the strain to failure was usually reported in tables. Thus, correlations between fracture toughness and εupl are only included for the AM alloys. Additionally, some studies report 'ductility' as measured through a uniaxial compression test; such data was excluded from the current analysis.

Fracture toughness: Only mode I fracture initiation toughness (K_{Ic} or K_{JIc}) values evaluated using standard fracture specimens (compact-tension [C(T)], single-edge bend [SE(B)], disk-shaped compact [DC(T)] configurations) were considered where K_{Ic} values were obtained directly from tests in accordance with ASTM standard E399 standard [19] or when K_{JIc} values were calculated from J-integral based crack resistance (R-curve) measurements in accordance with ASTM standard E1820 [20] using the J-K equivalence relationship, $K_{JIc} = (E' \times J_{Ic})^{0.5}$, where $E' = E / (1 - \nu^2)$ under plane strain conditions. Importantly, only fracture toughness data obtained from fatigue precracked samples were used, as non-precracked samples overestimate fracture toughness results due to the insufficient stress concentration at the root of a notch. Also, it was verified whether the reported K_{Ic} or K_{JIc} values met the standard sample dimension requirements such that the ligament size, b, and the sample thickness, B, were $\geq 2.5\,(K_Q/\sigma_y)^2$ or $\geq 10\,(J_Q/\sigma_{flow})^2$ for ASTM E399 and E1820, respectively, to ensure sample size-independent values for direct comparison between individual studies; the flow stress, σ_{flow}, is the average between σ_y and σ_{UTS}. For simplicity, K_{JIc} values will hereafter be denoted as K_{Ic}.

3. Fracture toughness vs. strength, ductility, and strain to failure in AM alloys

Fig. 1a shows fracture toughness versus yield strength plots for Al- [16,17,[21], [22], [23], [24], [25]], Fe- [15,[26], [27], [28], [29], [30], [31], [32], [33], [34], [35], [36], [37], [38], [39], [40], [41], [42]], and Ti-based alloys [14,[43], [44], [45], [46], [47], [48], [49]] that were processed either conventionally (open symbols) or via an AM technique (closed symbols). While there is some correlation between the two properties for all three groups of materials, they spread more widely for the AM alloys than for those conventionally processed. Similarly, fracture toughness broadly correlates with ε_f for the three alloy groups, as shown in Fig. 1b; however, the distribution of the fracture toughness data is wider for the AM materials than for the conventionally processed alloys.

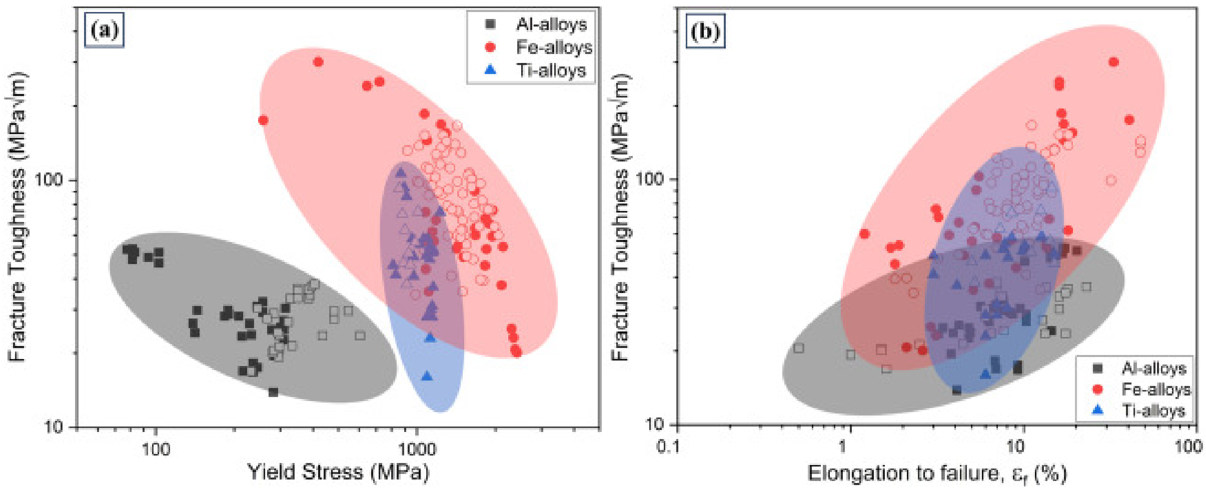

1. Download: Download high-res image (326KB)
2. Download: Download full-size image

Fig. 1. Correlation between (a) fracture toughness and yield strength, as well as (b) fracture toughness and elongation to failure for Al-, Fe-, and Ti-alloys that were either AM-processed (solid symbols) or conventionally fabricated (open symbols). Data for Al-alloys was taken from [16,17,[21], [22], [23], [24], [25]], for Fe-based materials from [15,[26], [27], [28], [29], [30], [31], [32], [33], [34], [35], [36], [37], [38], [39], [40], [41], [42]], and for Ti-alloys from [14,[43], [44], [45], [46], [47], [48], [49]]; only literature satisfying the data curation process was used to plot the graphs.

3.1. *Al-alloys*

3.1.1. Quantitative correlations between ductility and fracture toughness

Aluminum alloys, with their high strength-to-weight ratio, good corrosion resistance, and reasonable weldability, are key materials in industries such as automotive, aerospace, and defense. Processing complex-shaped parts and components used in these fields can achieve significant benefits from the versatile design capabilities provided by the various AM technologies [50]. However, high strength aluminum alloys are also well known for having relatively low fracture toughness, making its accurate evaluation highly important for many engineering designs. Fig. 2a shows how fracture toughness and ε_f of AM and conventionally processed Al-alloys, as well as both combined, correlate. It should be noted that most of the data is from the AM Al-Si and Al-Si-Mg alloy systems, whereas the data for conventionally processed alloys is taken from the different series of commercial Al-alloys. While there is a positive trend between the two properties for both manufacturing routes, their correlations are – individually as well as combined – weak, as indicated by the low coefficient of determination, R^2, values.

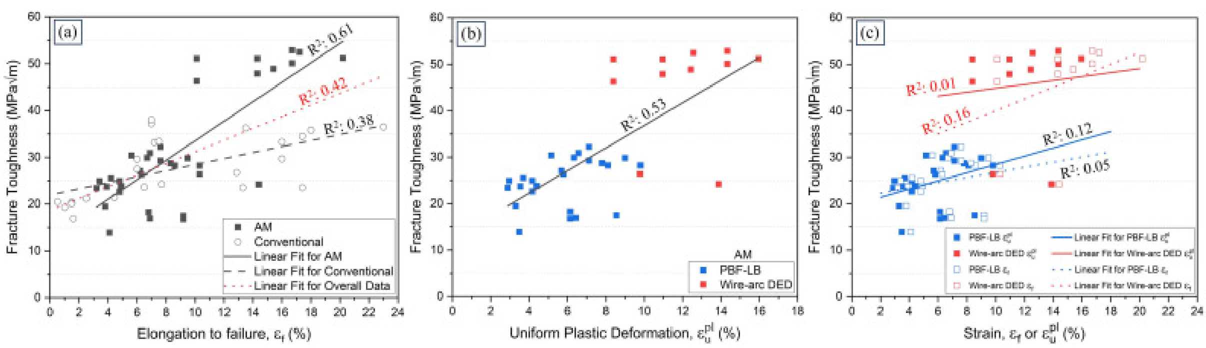

1. Download: Download high-res image (419KB)
2. Download: Download full-size image

Fig. 2. Correlations between (a) fracture toughness and elongation to failure, ε_f, for Al-alloys processed by conventional and AM methods and (b) fracture toughness and uniform plastic deformation, εupl, for AM processed Al-based alloys. In (c), separate fits and coefficients of determination, R^2 are shown for the different AM processes (PBF-LB and wire-arc DED) using both ε_f (open symbols) and εupl (closed symbols). Data was taken from [16,17,[21], [22], [23], [24], [25]].

For the AM-processed Al-alloys, the correlation between fracture toughness and the uniform plastic deformation strain, εupl, is also weak, as shown in Fig. 2b. Ductility is an especially poor indicator of the fracture toughness at intermediate ductility values (e.g., $\varepsilon_f \sim 10\%$ or εupl ~ 8%), where K_{Ic} values can vary between ~17 and 50 MPa√m. Next, Fig. 2c illustrates the challenge faced by researchers trying to optimize AM processing parameters for useful combinations of mechanical properties based solely on tensile test results. For PBF-LB processing, the correlation between fracture toughness and ductility is only $R^2 = 0.05$ when using the commonly reported value of ε_f and only improves slightly to $R^2 = 0.12$ when considering then correlation with εupl. Similarly poor correlations are seen for wire-arc DED where R^2 values of 0.16 and 0.01 are seen for fracture toughness correlations with ε_f and εupl, respectively. Overall, optimizing the AM processing parameters to achieve high combinations of strength and ductility will not indicate the optimal combination of strength and fracture toughness that is desired for engineering designs.

3.1.2. Mechanistic reasons for the poor correlations in AM fabricated Al-alloys

One contributor to high fracture toughness seen in Fig. 2 is the chosen AM technique whereby the alloys with K_{Ic} ~ 50 MPa√m were processed using wire-arc DED, and all others by PBF-LB. But it is also important to acknowledge how different processing parameters, test orientations, and other factors impact ductility and fracture toughness differently. De Menezes et al., for example, reported significant differences in fracture toughness based on the test orientation with K_{Ic} values for as-built PBF-LB-processed A357 (AlSi7Mg) ranging from ~16–32 MPa√m despite the reported ε_f for all orientations being within ~6.9 to 7.6% [21]. In contrast to that, we demonstrated in our own work on AlSi10Mg, processed by PBF-LB with different processing parameters but constant energy density, a reasonably good correlation between ε_f (ranging between ~3.2–6.9% for different testing orientations) and fracture toughness (which ranged from ~20–30 MPa√m) [16]. While both studies showed a wide range of measured fracture toughness values across the different orientations, a key difference was seen in the range of ε_f. The relatively wide range of ε_f observed in our work was primarily associated with differences in hatch spacing and layer thickness that impact grain size, grain orientation, cellular morphology, and melt pool arrangement and, as such, result in pronounced anisotropy. Tensile samples tested along the build direction showed more pronounced strain hardening, resulting in premature failure along the melt pool boundaries at $\varepsilon_f \sim 3.5\%$, compared to ~5–7% for the orthogonal loading direction (Fig. 3c). In contrast, De Menezes et al. reported some anisotropy in σ_y associated with crystallographic texture due to the thermal gradients that arise during printing, but the test orientation had relatively little effect on ε_f. The difference in the range of ε_f observed in these two studies is caused by differences in the Si composition that affect the morphology of the melt pool boundaries. In AlSi10Mg, a higher Si concentration results in wider melt pool boundaries, characterized by a coarser cellular region and a heat-affected zone (HAZ) [16], compared to the narrow melt pool boundaries in A357 (AlSi7Mg) that exhibit only a HAZ [21,51]. The width of the melt pool boundaries significantly impacts ε_f depending on the testing orientation, thereby controlling anisotropy during tensile testing. However, these melt pool boundaries, independent of their width, have a significant effect on the fracture toughness due to localized stress concentration that occurs near the crack tip, resulting in large anisotropy in K_{Ic} values, as seen in AlSi10Mg as well as in A357. The ranges in fracture toughness in both PBF-LB studies was primarily attributed to crack path tortuosity caused by crack deflections along the melt pool boundaries, as shown in Fig. 3 a,b, and hence more pronounced for cracks that grow parallel to the build direction, Fig. 3a, as compared to the orthogonal testing orientation, Fig. 3b. This results in significantly different *R*-curves, as indicated in Fig. 3c. We have shown that ductility (and strength) in AlSi10Mg – particularly parallel to the build direction – are controlled by the structure of the melt pool boundary and the formation of dimples that lead to failure [16]. Such crack path tortuosity is not expected to impact the strain to failure significantly, and thus the variability in fracture toughness should not be expected to correlate well to ductility.

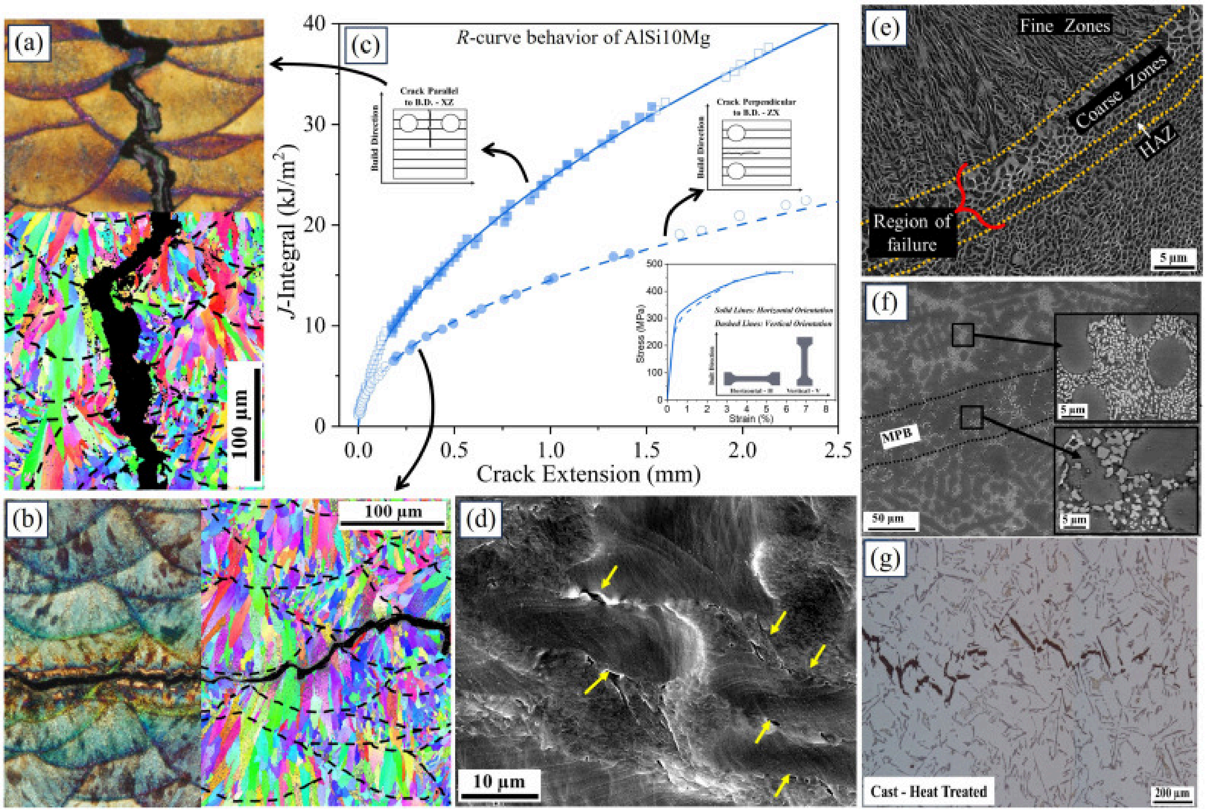

1. Download: Download high-res image (2MB)
2. Download: Download full-size image

Fig. 3. Crack propagation path (a) parallel and (b) perpendicular to the build direction in PBF-LB processed AlSi10Mg alloys; (c) crack resistance curve behavior with respect to testing direction with the corresponding tensile test results shown in the inset; (d) micrograph indicating crack initiation along the interface of α-Al dendrites and eutectic Al-Si in wire-arc DED-processed Al-Si alloy; micrographs of (e) AlSi10Mg alloys processed using PBF-LB and (f) Al-Si alloys processed using wire-arc DED; (g) crack propagation in cast Al-Si material. Images are reproduced with permission from Elsevier [16,24].

The reported fracture toughness values of the wire-arc DED-processed Al-Si with a compositional gradient of ~6.5–9.5% Si are in excess of ~50 MPa√m, over a ductility range between ~8–15%, as shown in Figs. 2b,c. This example represents a third situation where a wide range of ductility is observed over a small K_{Ic} range. These Al-Si alloys exhibit a combination of a dendritic microstructure and a coarse mesostructure that enables combinations of high K_{Ic} values and large ductility over a wide range which is primarily associated with differences in the Si-concentration at various tested locations. In tensile tests, upon plastic deformation, failure initiates in the form of microcracks along the interface of α-Al dendrites and eutectic Al-Si phases (that form both at the melt pool boundaries and inside the melt pools) due to a mismatch in their local strain deformation capacity [24], as shown in Fig. 3d. The volume fractions of these microstructural features and their spatial dimensions, which are controlled by the Si concentration, govern strain to failure. Fracture toughness, on the other hand, is not significantly influenced by the Si concentration, as crack propagation occurs through the formation of microcracks by decohesion of Si particles in the eutectic Al-Si, which, subsequently, results in crack bridging. This indicates that the size of the Si particles in the eutectic Al-Si (∼2–4 μm and ∼0.7–1 μm inside the melt pool boundary and the melt pool, respectively) and their spatial distribution influence crack initiation and fracture toughness rather than the volume fraction of the Si particles.

Comparing the micro- and meso-structures of the two AM methods (PBF-LB and wire-arc DED), structural features ranging from 200–600 nm cell structures are seen in PBF-LB alloys, shown in Fig. 3e, while coarse mm-sized mesostructures are seen in wire-arc DED-processed material with Si-particles ranging between ∼0.7–4.5 μm embedded in the eutectic Al-Si, shown in Fig. 3f. These very different characteristics are governed by the distinct cooling rates of the two AM processes combined with the low melting points of Al-alloys [52]. Conventionally processed, for example cast, Al-Si alloys, typically exhibit large dendrites with Si flakes or needles in the range of 100–200 μm, as indicated in Fig. 3g [53]. While these Si particles enhance the material's strength through precipitation hardening, they can also act as stress concentrations that result in cracks (Fig. 3g) and reduce the fracture toughness of the material. This behavior is also seen in heat-treated PBF-LB alloys that exhibit μm-sized Si particles that act as stress concentrations and reduce fracture toughness from ∼30 MPa√m to ∼17 MPa√m while ductility remains essentially the same [23]. As a result, similar to wire-arc DED-processed Al-Si, the volume fraction and size of the Si particles may impact the strength, fracture toughness, and ε_f differently in these materials depending on the microstructural details and the active damage mechanisms.

3.2. *Fe-based alloys*

3.2.1. Quantitative correlations between ductility and fracture toughness

Fig. 4a shows the correlation between fracture toughness and (reported) ε_f for AM and conventionally processed Fe-based alloys, as well as their combined correlation, indicating a weak positive correlation (i.e., low R^2 values from 0.28 to 0.55) between these properties. The correlation between fracture toughness and the uniform plastic deformation strain, εupl, is also weak across the various AM produced steels as shown in Fig. 4b. Next, Fig. 4c illustrates the issue with trying to optimize PBF-LB processing parameters for useful combinations of steel mechanical properties based solely on tensile test results. In Fig. 4c, only the PBF-LB results are shown due to the limited data for other methods. The correlation between fracture toughness and ductility is R^2 = 0.57, when the commonly reported values of ε_f are used and only R^2 = 0.0004 when εupl is considered. Similar to the findings for AM fabricated Al-alloys, the lack of correlation is apparent at intermediate ductility levels (e.g., ε_f ∼ 15% or εupl ∼ 10%) where K_{Ic} can be as high as 240–250 MPa√m for wire-arc DED produced high-strength low-alloy (HSLA) steels [26] and as low as 62–69 MPa√m for direct metal laser sintered (DMLS) fabricated 15–5 PH stainless steel [42]. Also, such results are similar to past reports on conventionally processed high-strength steels [[4], [5], [6],54] that have shown that there is no reasonable correlation between fracture toughness and any uniaxial tensile stress-strain properties and that no ductility parameter can be considered as a reliable indicator of fracture toughness.

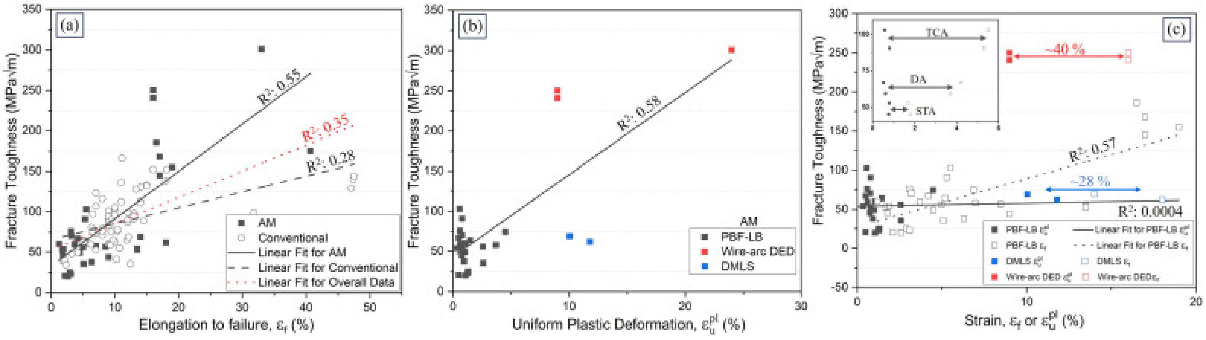

1. [Download: Download high-res image (391KB)]
2. [Download: Download full-size image]

Fig. 4. Correlations between (a) fracture toughness and elongation to failure in Fe-based alloys processed through both conventional and AM methods and (b) fracture toughness and uniform plastic deformation, εupl, for AM processed Fe-based alloys. In (c), separate fits and coefficients of determination, R^2, are shown for the different AM processes (PBF-LB and wire-arc DED) using both ε_f (open symbols) and εupl (closed symbols); inset in (c) shows the difference in ε_f and εupl for PBF-LB processed maraging steels that have undergone different heat treatments: solutionized + aged (STA), directly aged (DA), or thermal cycling (TCA). Data was taken from [15,[26], [27], [28], [29], [30], [31], [32], [33], [34], [35], [36], [37], [38], [39], [40], [41]].

3.2.2. Mechanistic reasons for the poor correlations in AM fabricated steels

The wide spread in fracture toughness at similar, intermediate ductility levels of ~10% εupl, Fig. 4b, is the result of differences in the materials' microstructures that derive from the specific AM method that has been used and that affect the two properties differently. The combination of low εupl and high K_{Ic} data is from the wire-arc DED-processed high-strength low-alloy (HSLA) structural steels [26] that are precipitation-hardened, contain low amounts of alloying elements, e.g., 0.05–0.25% C, and exhibit a microstructure of primarily austenite and ferrite. In contrast, the data from the material that is similarly ductile but exhibits much lower K_{Ic} is from studies on the direct metal laser sintered (DMLS) 15–5 PH stainless steel [42], which is a precipitation-hardened martensitic stainless steel with ~15% Cr and 5% Ni. While ductility and fracture toughness in these alloys do not correlate, K_{Ic} seems to weakly correlate with the fraction of strain in the necking region (i.e., $\varepsilon_f - \varepsilon_{UTS}$ in Fig. A1) to the total strain, and which is indicated by the red arrow in Fig. 4c for the wire-arc DED-processed material and by the blue arrow for the DMLS-processed material. The reason for this is that the plastic zone at the crack tip more closely resembles necking than uniform elongation. The wire-arc DED-processed HSLA steel with high fracture toughness, for example, exhibits more stable plastic deformation (~40% of ε_f, indicated by the red arrow in Fig. 4c) after the onset of necking than the DMLS 15–5 PH steel that has a lower fracture toughness and where stable plastic deformation accounts for ~28% of ε_f, shown as blue arrow in Fig. 4c. This observation, once again, emphasizes the importance of assessing fracture toughness rather than solely relying on strength and ductility in these materials as strain, particularly after the onset of necking, is dependent on not only sample size but also the location where it is measured.

PBF-LB-processed maraging steels generally have been reported to have similar uniform plastic deformation strain below 5% while the K_{Ic} values range between 20–100 MPa√m [15,27,30,31]. This is associated with differences in process parameter-controlled cellular, micro- and meso-structures as well as varying heat treatments and, hence, differences in the microstructural phases and their fraction. In the as-built condition, these materials exhibit a cellular microstructure, shown in Fig. 5a, with a network of dislocations formed by the segregation of solute elements like Mo, Ti, Al, and Ni, together with minor fractions of retained austenite at the cell boundaries [31,[55], [56], [57]] which impact εupl and ε_f differently. For example, AM maraging steel that has been subjected to a solution treatment at 1000 ºC for 1 hour followed by aging at 480 ºC for 6 hours, which has been shown to decompose the cellular structures, as shown in Fig. 5b, exhibits uniform elongation comparable to the material that was directly aged at 480 ºC for 6 hours (~0.5–0.7%), which retained its cellular and mesostructural features, as shown in Fig. 5c [30]. However, strain from the onset of necking to failure (i.e., $\varepsilon_f - \varepsilon_{UTS}$) is considerably more in the directly aged condition than in the solution treated + aged material, as shown by the black arrows in the inset of Fig. 4c, which is associated with the cellular features acting as soft barriers that stabilize dislocation motion and as such delay failure [56]. This, as mentioned before, impacts fracture toughness, resulting in a K_{Ic} of ~67 MPa√m for samples that are directly aged (DA) compared to K_{Ic} ~ 45 MPa√m for the solutionized + aged material (STA), despite both having similar ductility [30]. Additionally, segregation during aging enables austenite stabilizers like Ni to promote the reverse transformation of martensite into austenite partially decomposing the cellular microstructure, shown in Fig. 5d, which, while decreasing strength, enhances plasticity [30,58,59]. We have shown that heat treatments such as thermal cycling (TCA), specifically designed to trigger the reverse transformation of austenite, can increase the fracture toughness of the material as crack tip stresses during crack growth can then induce transformation-induced plasticity (TRIP) through the transformation of austenite into martensite, indicated in Fig. 5e,f; this enables enhanced crack growth resistance, shown in Fig. 5g, with K_{Ic} values in excess of 100 MPa√m. While the TRIP effect enhances the fracture toughness, it is often only triggered close to or at σ_{UTS} so that ductility of the material remains comparable to the peak-aged condition with 0.5–0.6% [30]. In contrast, certain heat treatments such as aging the material at 530 ºC for 3 hours can have a negative impact on fracture toughness reducing K_{Ic} to ~20 MPa√m. The reason for this is a lack of austenite combined with oxidation-induced embrittlement, which, however, has also only a limited impact on ductility which remained comparable to that for the highest reported K_{Ic} values [31]. Thus, steels are an excellent example where metastable phases formed during the AM processes and subsequent post heat treatments can play a strong role in causing the lack of correlation between fracture toughness and ductility.

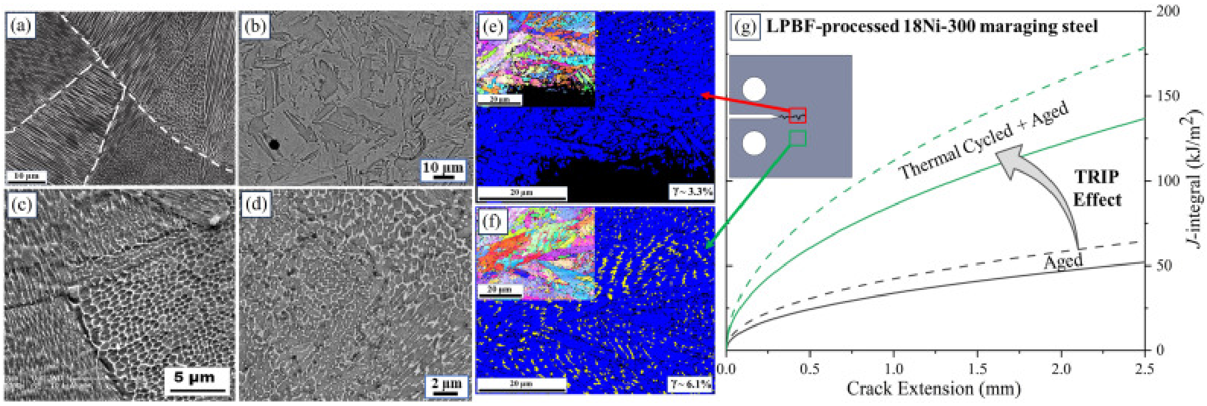

1. Download: Download high-res image (1MB)

2. Download: Download full-size image

Fig. 5. (a) Microstructure of as-built PBF-LB-processed maraging steel and (b-d) after different heat-treatments; (e,f) EBSD crack path analyses indicating the TRIP effect contributing to the (g) increase in the crack growth resistance after thermal cycling + aging. Images are reproduced with permission from Elsevier [15,30].

3.3. *Ti-6Al-4V (Ti64)*

3.3.1. Quantitative correlations between ductility and fracture toughness

Similar to Al and Fe-based alloys, there is a very weak correlation between fracture toughness and ε_f for the AM and conventionally processed Ti64, both individually and combined, as shown in Fig. 6a. There is zero correlation between fracture toughness and uniform deformation strain for PBF-LB processed Ti64, as shown in Fig. 6b. It should be noted that due to our data selection criteria, the data points shown in Fig. 6b are limited to only two studies using the PBF-LB method [14,43]. Moreover, Fig. 6 demonstrates how optimizing PBF-LB processing parameters to achieve high combinations of strength and ductility for Ti64 may not always be helpful for finding the optimal combination of strength and fracture toughness that is desired for engineering designs.

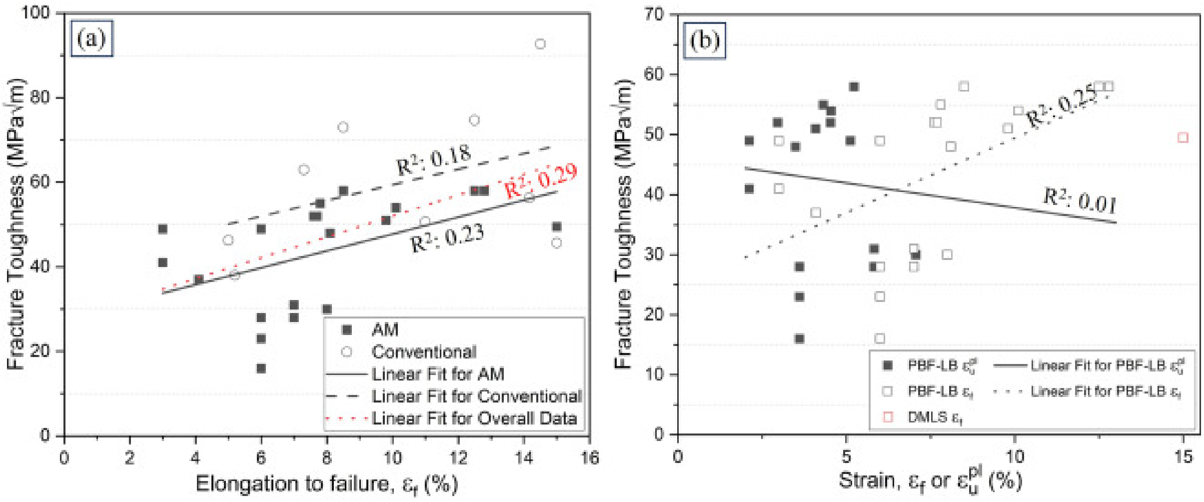

1. Download: Download high-res image (321KB)
2. Download: Download full-size image

Fig. 6. Correlations between (a) fracture toughness and elongation to failure in Ti64 alloys processed through both conventional and AM methods and (b) fracture toughness and ductility in PBF-LB processed Ti64 alloys. Data was taken from [14,[43], [44], [45], [46], [47], [48], [49]].

3.3.2. Mechanistic reasons for the poor correlations in PBF-LB fabricated Ti64

Over the entire ductility range, the K_{Ic} values of the AM-processed Ti64 range between 16–58 MPa√m in the as-built condition. The poor correlation in the data could be attributed to the following three factors. (a) Low work hardening in Ti64. The near-perfectly plastic tensile response of Ti64 makes stress and strain in the plastic regime uncorrelated and, hence, strain to failure more sensitive to other microstructural parameters (such as porosity and grain texture) and specimen geometry. (b) Epitaxial growth of the grains under certain processing conditions, which makes them columnar and, in turn, causes the mechanical properties to be highly anisotropic. Such anisotropy often has different consequences for ductility and fracture toughness. (c) Porosity that forms during processing. While porosity is known to have a negative impact on ductility for many classes of materials, its effect on fracture toughness varies between materials. In Al-alloys, porosity can lead to enhanced fracture toughness through localized blunting and crack deflections [24], whereas in Ti64, porosity significantly compromises fracture toughness, primarily due to the alloy's limited strain hardening capacity. For PBF-LB-processed Ti64 with ductility ranging between ~3–5%, Cain et al., for example, reported K_{Ic} values ranging from 16–28 MPa√m [43], whereas Kumar et al. measured K_{Ic} values between 48–58 MPa√m, which has been associated with the relatively lower porosity in their material [14]. Additionally, AM scan strategies such as a chessboard pattern – where small "islands" within a single layer are printed in various directions as an approach to reduce residual stresses – have been shown to lead to the formation of pores aligned with the scan direction, as shown in Fig. 7a, which promotes anisotropy in the material and may be among the main reasons for the large variations in fracture toughness despite otherwise similar microstructure characteristics [14,43,60].

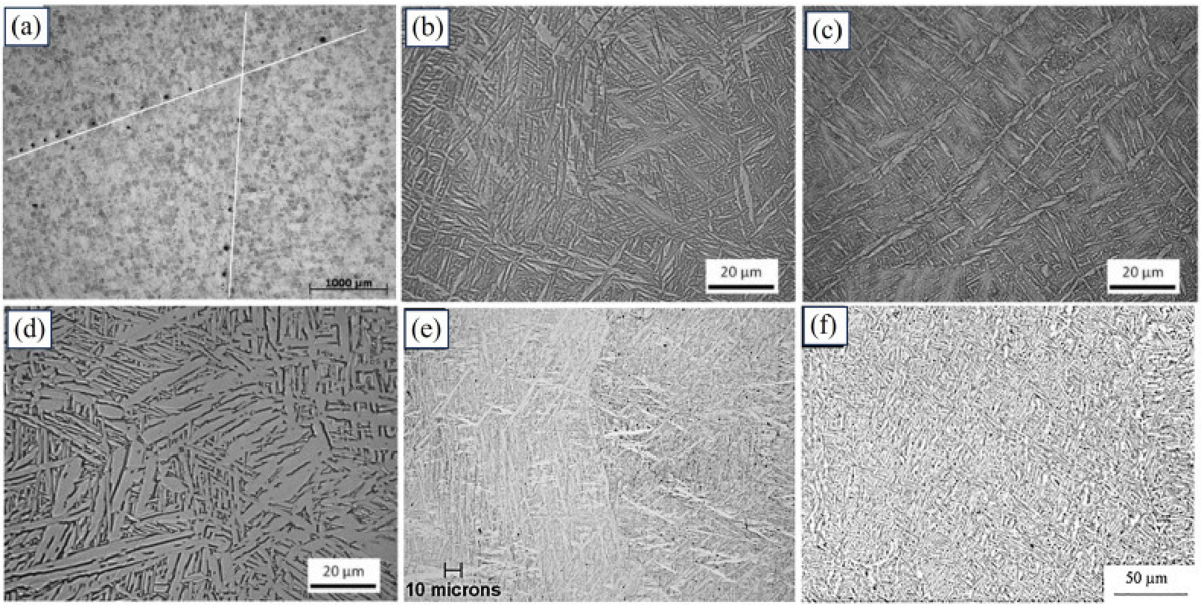

1. Download: Download high-res image (1MB)
2. Download: Download full-size image

Fig. 7. (a) Pores that form during printing, are aligned along the scan track; (b) microstructure of as-built PBF-LB-processed Ti6Al4V; microstructure changes with heat treatments (c) above and (d) below the β transus temperature; microstructure of as-built Ti6Al4V processed by (e) DED and (f) PBF-EB. Images are reproduced with permission from Elsevier and Wiley [43,60,61].

In addition to porosity, unique microstructural features that span across multiple length scales impact the mechanical properties of AM-Ti64. PBF-LB-processed material in the as-built condition, for example, primarily consists of a fine α'-lath microstructure within the prior-β grains that are mesostructured (Fig. 7b); the size of the laths and the texture introduced by the prior-β grains play a significant role on both ductility and fracture toughness. During tensile testing, failure in Ti64 alloys often occurs along the columnar prior-β grain boundaries indicating that the shape and size of prior-β grains control ε_f [14]. Based on the Ritchie–Knott–Rice (RKR) micromechanical model [62], fracture toughness, however, is associated with a characteristic microstructural length scale, l^* which, in the case of Ti64 alloys, is related to the size of the α'/α laths [14]. For example, work on the impact of processing parameters on the mechanical properties of PBF-LB-Ti64 shows that batches of material with significantly different size and shape of the prior-β grains exhibit ε_f varying between ~7–13%; fracture toughness, however, remains consistent with K_{Ic} values of ~ 48–58 MPa√m which is associated with the uniform lath size of ~1 µm for all batches [14].

Thermal post-processing can be used to control the size, shape, and fraction of the α and β phases and, as such, control the spread in the fracture toughness data. Post-processing aimed to stress relieve PBF-LB-processed material, for example, has shown that heat-treatments below the β transus temperature (T_{β}) partially decompose the α' martensite structure into a coarsened acicular α phase, indicated in Fig. 7c, while retaining the prior-β grains and hence the mesostructure. Compared to that, heat-treatments above T_{β} lead to the formation of β which, upon subsequent cooling, develops into the Widmanstätten α/β structure, shown in Fig. 7d; this transformation is strongly linked to the cooling rate. While coarsening of the α-laths or the formation of the Widmanstätten α/β structure can increase ductility, such microstructure modifications impact fracture toughness significantly. In the Cain et al. work, for example, fracture toughness increased from 16–28 MPa√m in the as-built condition to 41–49 MPa√m after heat-treatment, while ductility remained essentially the same (or in some cases even degraded) [43].

PBF-LB-Ti64 microstructure characteristics are distinct to those from other AM-techniques primarily due to differences in heat transfer and hence, cooling rate. Fig. 7b,e,f shows α and β microstructures that often form during processing using different AM methods. The as-built microstructures of PBF-LB and DED-processed material, Fig. 7b and Fig. 7e, respectively, are characterized by the fine needle-shaped α' martensite, typically with a lath width of 0.2–1 μm. Compared to that, material processed using PBF-EB, Fig. 7f, often has an α + β dual phase, where the α-lath has an average length and thickness of 1–3 μm and 0.5–1 μm, respectively, while the β-platelets are often ~0.1 μm thick [61]. While numerous studies on Ti64 processed by PBF-EB, DMSL, and DED focus on the materials' ductility [8,61,63,64], there is limited work on fracture toughness and most of the samples used in these studies are not sufficiently large to provide size-independent fracture toughness data. Further work is required to fully understand the effect of α and β microstructures, which differ for the various AM methods and feature unique α'/α lath sizes, on fracture toughness.

4. Impact of deformation and toughening mechanisms on ductility and fracture toughness

The above sections highlight examples of how microstructural features and plastic deformation characteristics impact both the tensile stress-strain response and the fracture toughness, but often in different ways. Detailed structure-property relationships, therefore, should be developed with the careful consideration of all the factors that could affect these properties. In that regard, another consideration worthy of discussion is the sequence of plastic deformation mechanisms. Whether deformation mechanisms, such as dislocation multiplication and twinning- and transformation-induced plasticity (TWIP, TRIP), are activated either simultaneously or sequentially can have a dramatic impact on the strain hardening capacity of a material [[65], [66], [67]]. However, while an early activation of, e.g., TRIP during testing may create brittle phases that act as stress concentrations that cause crack deflection but can also decrease crack growth resistance, this may, simultaneously, contribute to plastic deformation, enhancing ductility. Compared to that, the activation of TRIP close to or after reaching the ultimate tensile strength – after the onset of necking – may not accurately reflect the impact of plasticity on the crack tip during fracture toughness testing [30], as tensile strain measurements in this stage are highly sensitive to sample geometry. Similarly, micromechanisms such as the formation of shear and kink bands, which often occur during the necking stage of tensile tests, have the potential to significantly enhance fracture toughness by distributing damage at the crack tip without impacting ductility [68,69].

While discrepancies in the correlation between ductility and fracture toughness are apparent in many conventional alloys, they can be particularly pronounced in AM alloys. This is due to the interaction of deformation mechanisms with factors inherent to AM materials: (i) processing-related issues such as defects, porosity, and residual stresses, (ii) unique micro- and mesostructural characteristics that arise from the line-by-line and layer-by-layer nature of 'bottom up' processing, (iii) the formation of metastable phases and cellular structures due to rapid solidification, and (iv) the unique thermal histories experienced by the solidified AM alloy that occur during fabrication. While fracture toughness is to some extent related to the material's intrinsic capacity to absorb plastic energy (as indicated by the work of fracture that can be deducted from tensile tests but also shows an only weak correlation with fracture toughness, as indicated in Fig. A2), it is often also significantly influenced by extrinsic toughening mechanisms such as crack bridging or crack deflection, that act on a more localized scale and can be more pronounced in AM materials due to their unique structural features. Aside from that, it should be mentioned that the sensitivity to sample geometry during tensile testing may additionally impact the correlation between fracture toughness and ductility. Due to fabrication size constraints in AM research, many studies follow ASTM standard recommendations regarding gauge length-to-width or gauge length-to-(area$^{0.5}$) ratios rather than using full-size ASTM samples. While it is commonly accepted that gauge sections containing more than 100 grains should be sufficient to assess strength properties that can inform design parameters, additional factors such as the number of melt pool boundaries within the sample cross section should be considered when assessing their tensile stress-strain response. Furthermore, the use of shorter gauge lengths, even within the ASTM ratios, is known to result in elevated strain gradients that may, additionally, impact ductility [70] and hence could influence its correlation with fracture toughness.

5. Concluding remarks

While ductility is often used as an indicator for fracture toughness, the correlations between these two properties are weak for both AM and conventionally processed Al-, Fe-, and Ti-based alloys, and in some cases, there is essentially no correlation. Accordingly, care should hence be taken when optimizing AM processing parameters for structural applications solely based on strength and ductility. While ductility is an important property and critical to be assessed for applications that require excessive amounts of plasticity and deformability, parts and components for most engineering applications are designed based on yield strength and fracture toughness and, as a result, only require a modest amount of ductility if the fracture toughness is sufficient to provide adequate damage tolerance. Given the large spread in the fracture toughness data at intermediate ductility ranges, it is crucial to assess the failure characteristics of AM fabricated alloys in terms standardized fracture toughness measurements, (e.g., K_{Ic} or K_{JIc}), to fully understand how to best optimize the AM processing parameters for structural integrity and reliability.

CRediT authorship contribution statement

Moses J. Paul: Data curation, Formal analysis, Investigation, Visualization, Writing – original draft. **Jamie J. Kruzic:** Formal analysis, Investigation, Writing – review & editing. **Upadrasta Ramamurty:** Conceptualization, Formal analysis, Writing – review & editing. **Bernd Gludovatz:** Conceptualization, Formal analysis, Investigation, Project administration, Supervision, Validation, Writing – review & editing.

Declaration of competing interest

The authors declare that they have no known competing financial interests or personal relationships that could have appeared to influence the work reported in this paper.

Acknowledgements

MJP and UR acknowledge funding from A*STAR, Singapore via the Structural Metals and Alloys Programme (No. A18B1b0061) and BG acknowledges support from the ARC Future Fellowship (project number FT190100484) and the UNSW Scientia Fellowship schemes.

Appendix

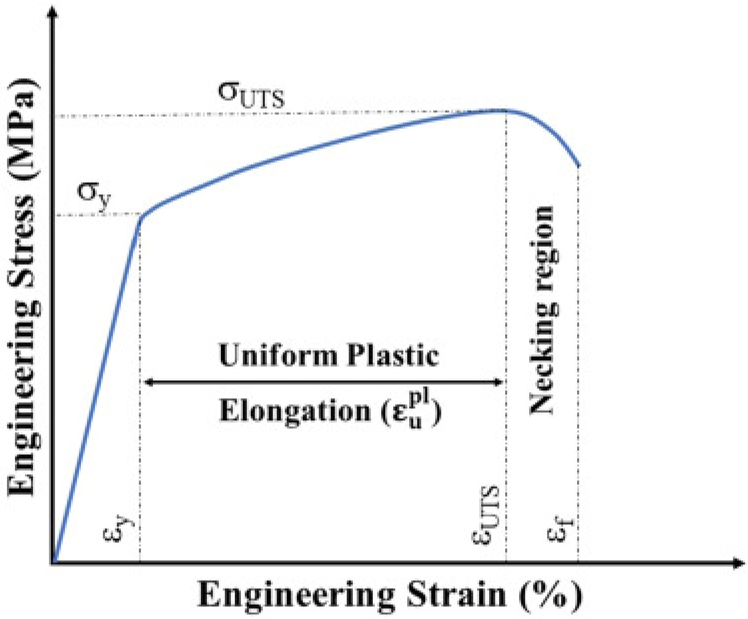

1. Download: Download high-res image (159KB)
2. Download: Download full-size image

Fig. A1. Schematic of tensile stress-strain data indicating yield, σ_y, and ultimate tensile strength, σ_{UTS}, as well as strain at yielding, ε_y, strain corresponding to tensile strength, ε_{UTS}, and failure strain, ε_f. Ductility is defined as the strain corresponding to uniform plastic elongation, εupl, from yielding to ε_{UTS}, i.e., $\varepsilon_{UTS} - \varepsilon_y$, and the necking region from the onset of necking to failure, i.e., $\varepsilon_f - \varepsilon_{UTS}$.

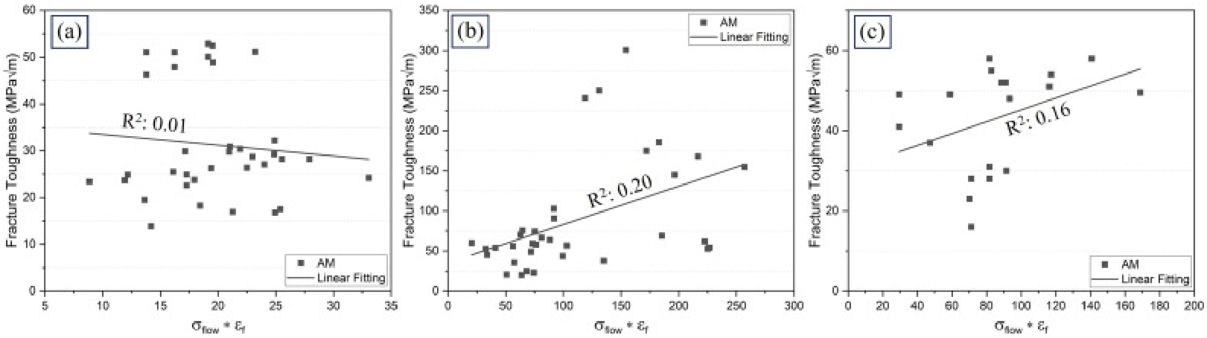

1. Download: Download high-res image (267KB)
2. Download: Download full-size image

Fig. A2. Correlation between fracture toughness and (σ_{flow}*ε_f), for (a) Al-, (b) Fe- and (c)Ti-based alloys processed using AM techniques and their corresponding R^2 values of the individual linear fits.

References

1. [1]

R.O. Ritchie

The conflicts between strength and toughness

Nat. Mater., 10 (2011), pp. 817-822, 10.1038/nmat3115

View in ScopusGoogle Scholar

2. [2]

S.Z. Han, E.A. Choi, S.H. Lim, S. Kim, J. Lee

Alloy design strategies to increase strength and its trade-offs together

Prog. Mater Sci., 117 (2021), Article 100720, 10.1016/j.pmatsci.2020.100720
View PDFView articleView in ScopusGoogle Scholar

3. [3]
E. Ma, T. Zhu
Towards strength–ductility synergy through the design of heterogeneous nanostructures in metals
Mater. Today, 20 (2017), pp. 323-331, 10.1016/j.mattod.2017.02.003
View PDFView articleView in ScopusGoogle Scholar

4. [4]
D. Frómeta, A. Lara, L. Grifé, T. Dieudonné, P. Dietsch, J. Rehrl, C. Suppan, D. Casellas, J. Calvo
Fracture resistance of advanced high-strength steel sheets for automotive applications
Metall. Mater. Trans. A, 52 (2021), pp. 840-856, 10.1007/s11661-020-06119-y
View in ScopusGoogle Scholar

5. [5]
Z. Xiong, P.J. Jacques, A. Perlade, T. Pardoen
Characterization and control of the compromise between tensile properties and fracture toughness in a quenched and partitioned steel
Metall. Mater. Trans. A, 50 (2019), pp. 3502-3513, 10.1007/s11661-019-05265-2
View in ScopusGoogle Scholar

6. [6]
G. Lacroix, T. Pardoen, P.J. Jacques
The fracture toughness of TRIP-assisted multiphase steels
Acta Mater., 56 (2008), pp. 3900-3913, 10.1016/j.actamat.2008.04.035
View PDFView articleView in ScopusGoogle Scholar

7. [7]
J.J. Kruzic
Bulk metallic glasses as structural materials: a review
Adv. Eng. Mater., 18 (2016), pp. 1308-1331, 10.1002/adem.201600066
View in ScopusGoogle Scholar

8. [8]
J.J. Lewandowski, M. Seifi
Metal additive manufacturing: a review of mechanical properties
Annu. Rev. Mater. Res., 46 (2016), pp. 151-186, 10.1146/annurev-matsci-070115-032024
View in ScopusGoogle Scholar

9. [9]
W.E. Frazier
Metal additive manufacturing: a review
J. Mater. Eng. Perform., 23 (2014), pp. 1917-1928, 10.1007/s11665-014-0958-z
View in ScopusGoogle Scholar

10. [10]
D. Herzog, V. Seyda, E. Wycisk, C. Emmelmann
Additive manufacturing of metals
Acta Mater., 117 (2016), pp. 371-392, 10.1016/j.actamat.2016.07.019
View PDFView articleView in ScopusGoogle Scholar

11. [11]

Y.M. Wang, T. Voisin, J.T. McKeown, J. Ye, N.P. Calta, Z. Li, Z. Zeng, Y. Zhang, W. Chen, T.T. Roehling, R. T. Ott, M.K. Santala, P.J. Depond, M.J. Matthews, A.V. Hamza, T. Zhu
Additively manufactured hierarchical stainless steels with high strength and ductility
Nat. Mater., 17 (2017), pp. 63-71, 10.1038/nmat5021
View in ScopusGoogle Scholar

12. [12]
P. Bajaj, A. Hariharan, A. Kini, P. Kürnsteiner, D. Raabe, E.A. Jägle
Steels in additive manufacturing: a review of their microstructure and properties
Mater. Sci. Eng.: A, 772 (2020), Article 138633, 10.1016/j.msea.2019.138633
View PDFView articleView in ScopusGoogle Scholar

13. [13]
P. Kumar, U. Ramamurty
Microstructural optimization through heat treatment for enhancing the fracture toughness and fatigue crack growth resistance of selective laser melted Ti–6Al–4V alloy
Acta Mater., 169 (2019), pp. 45-59, 10.1016/j.actamat.2019.03.003
View PDFView articleGoogle Scholar

14. [14]
P. Kumar, O. Prakash, U. Ramamurty
Micro-and meso-structures and their influence on mechanical properties of selectively laser melted Ti-6Al-4V
Acta Mater., 154 (2018), pp. 246-260, 10.1016/j.actamat.2018.05.044
View PDFView articleView in ScopusGoogle Scholar

15. [15]
J. Suryawanshi, K.G. Prashanth, U. Ramamurty
Tensile, fracture, and fatigue crack growth properties of a 3D printed maraging steel through selective laser melting
J. Alloys Compd., 725 (2017), pp. 355-364, 10.1016/j.jallcom.2017.07.177
View PDFView articleView in ScopusGoogle Scholar

16. [16]
M.J. Paul, Q. Liu, J.P. Best, X. Li, J.J. Kruzic, U. Ramamurty, B. Gludovatz
Fracture resistance of AlSi10Mg fabricated by laser powder bed fusion
Acta Mater., 211 (2021), Article 116869, 10.1016/j.actamat.2021.116869
View PDFView articleView in ScopusGoogle Scholar

17. [17]
Q. Liu, H. Wu, M.J. Paul, P. He, Z. Peng, B. Gludovatz, J.J. Kruzic, C.H. Wang, X. Li
Machine-learning assisted laser powder bed fusion process optimization for AlSi10Mg: New microstructure description indices and fracture mechanisms
Acta Mater., 201 (2020), pp. 316-328, 10.1016/j.actamat.2020.10.010
View PDFView articleGoogle Scholar

18. [18]
J. Suryawanshi, K.G. Prashanth, S. Scudino, J. Eckert, O. Prakash, U. Ramamurty
Simultaneous enhancements of strength and toughness in an Al-12Si alloy synthesized using selective laser melting
Acta Mater., 115 (2016), pp. 285-294, 10.1016/j.actamat.2016.06.009

View PDFView articleView in ScopusGoogle Scholar

19. [19]

ASTM Standard E399, Standard test method for linear-elastic plane-strain fracture toughness KIc of metallic materials, 2022. https://doi.org/10.1520/E0399-22.

Google Scholar

20. [20]

ASTM Standard E1820, Standard Test Method for Measurement of Fracture Toughness, 2018. https://doi.org/10.1520/E1820-18.

Google Scholar

21. [21]

J.T. Oliveira de Menezes, E.M. Castrodeza, R. Casati

Effect of build orientation on fracture and tensile behavior of A357 Al alloy processed by selective laser melting

Mater. Sci. Eng.: A, 766 (2019), Article 138392, 10.1016/j.msea.2019.138392

View PDFView articleView in ScopusGoogle Scholar

22. [22]

T. Klein, T. Wojcik, A. Arnoldt

A hypoeutectic Al-Ni-Mg in situ composite processed by wire-arc additive manufacturing: Phase evolution and mechanical behavior

Mater. Des., 222 (2022), Article 111066, 10.1016/j.matdes.2022.111066

View PDFView articleView in ScopusGoogle Scholar

23. [23]

J.T.O. de Menezes, E.M. Castrodeza, L. Patriarca, R. Casati

Effect of heat treatments and loading orientation on the tensile properties and fracture toughness of AlSi7Mg alloy produced by Laser Powder Bed Fusion

Int. J. Fract., 235 (2022), pp. 145-157, 10.1007/s10704-022-00631-5

View in ScopusGoogle Scholar

24. [24]

M.J. Paul, T. Klein, C. Simson, J. Niedermayer, J.J. Kruzic, B. Gludovatz

Strength and fracture resistance of in-situ alloyed compositionally-graded Al-Si processed by dual-wire arc directed energy deposition

Addit. Manuf., 60 (2022), Article 103291, 10.1016/j.addma.2022.103291

View PDFView articleView in ScopusGoogle Scholar

25. [25]

J.G. Kaufman, E.L. Rooy

Aluminum Alloy Castings : Properties, processes, and Applications

ASM International (2004)

Google Scholar

26. [26]

P. Dirisu, S. Ganguly, A. Mehmanparast, F. Martina, S. Williams

Analysis of fracture toughness properties of wire + arc additive manufactured high strength low alloy structural steel components

Mater. Sci. Eng.: A, 765 (2019), Article 138285, 10.1016/j.msea.2019.138285

View PDFView articleView in ScopusGoogle Scholar

27. [27]
P.L.L. Santos, J.A. Avila, E.B. da Fonseca, A.H.G. Gabriel, A.L. Jardini, É.S.N. Lopes
Plane-strain fracture toughness of thin additively manufactured maraging steel samples
Addit. Manuf., 49 (2022), Article 102509, 10.1016/j.addma.2021.102509
View PDFView articleView in ScopusGoogle Scholar
28. [28]
M. Abdelwahed, S. Bengtsson, M. Boniardi, A. Casaroli, R. Casati, M. Vedani
An investigation on the plane-strain fracture toughness of a water atomized 4130 low-alloy steel processed by laser powder bed fusion
Mater. Sci. Eng.: A, 855 (2022), Article 143941, 10.1016/j.msea.2022.143941
View PDFView articleView in ScopusGoogle Scholar
29. [29]
K.S. Prakash, A.R. Kannan, R. Pramod, N.P. Kumar, N.S. Shanmugam
Microstructure, mechanical properties and fracture toughness of SS 321 stainless steel manufactured using wire arc additive manufacturing
Trans. Indian Inst. Met., 76 (2023), pp. 537-544, 10.1007/s12666-022-02713-3
View in ScopusGoogle Scholar
30. [30]
M.J. Paul, Y. Muniandy, J.J. Kruzic, U. Ramamurty, B. Gludovatz
Effect of heat treatment on the strength and fracture resistance of a laser powder bed fusion-processed 18Ni-300 maraging steel
Mater. Sci. Eng.: A, 844 (2022), Article 143167, 10.1016/j.msea.2022.143167
View PDFView articleView in ScopusGoogle Scholar
31. [31]
S. Wei, P. Kumar, K.B. Lau, D. Wuu, L.L. Liew, F. Wei, S.L. Teo, A. Cheong, C.K. Ng, B. Zhang, C.C. Tan, P. Wang, U. Ramamurty
Effect of heat treatment on the microstructure and mechanical properties of 2.4 GPa grade maraging steel fabricated by laser powder bed fusion
Addit. Manuf., 59 (2022), Article 103190, 10.1016/j.addma.2022.103190
View PDFView articleView in ScopusGoogle Scholar
32. [32]
E. Jelis, M.R. Hespos, N.M. Ravindra
Process evaluation of AISI 4340 steel manufactured by laser powder bed fusion
J. Mater. Eng. Perform., 27 (2018), pp. 63-71, 10.1007/s11665-017-2989-8
View in ScopusGoogle Scholar
33. [33]
H.F. Li, Q.Q. Duan, P. Zhang, X.H. Zhou, B. Wang, Z.F. Zhang
The quantitative relationship between fracture toughness and impact toughness in high-strength steels
Eng. Fract. Mech., 211 (2019), pp. 362-370, 10.1016/j.engfracmech.2019.03.003
View PDFView articleView in ScopusGoogle Scholar
34. [34]
V.X. De Lima Filho, T.N. Lima, S. Griza, B.R.C. Saraiva, H.F.G. De Abreu
The increase of fracture toughness with solution annealing temperature in 18Ni Maraging 300 steel

Mater. Res., 24 (2021), Article e20200472, 10.1590/1980-5373-mr-2020-0472
Google Scholar
35. [35]
G. Niu, H.S. Zurob, R.D.K. Misra, Q. Tang, Z. Zhang, M.T. Nguyen, L. Wang, H. Wu, Y. Zou
Superior fracture toughness in a high-strength austenitic steel with heterogeneous lamellar microstructure
Acta Mater., 226 (2022), Article 117642, 10.1016/j.actamat.2022.117642
View PDFView articleView in ScopusGoogle Scholar
36. [36]
H.F. Li, J.L. Wei, S.P. Yang, Y.Q. Liu
The relationship between fracture toughness and tensile property in high-strength steels
Eng. Fail. Anal., 131 (2022), Article 105854, 10.1016/j.engfailanal.2021.105854
View PDFView articleView in ScopusGoogle Scholar
37. [37]
J.I. Yoon, J. Jung, S.H. Joo, T.J. Song, K.G. Chin, M.H. Seo, S.J. Kim, S. Lee, H.S. Kim
Correlation between fracture toughness and stretch-flangeability of advanced high strength steels
Mater. Lett., 180 (2016), pp. 322-326, 10.1016/j.matlet.2016.05.145
View PDFView articleView in ScopusGoogle Scholar
38. [38]
R.O. Ritchie
Near-Threshold fatigue crack propagation in ultra-high strength steel: influence of load ratio and cyclic strength
J. Eng. Mater. Technol., 99 (1977), pp. 195-204, 10.1115/1.3443519
View in ScopusGoogle Scholar
39. [39]
L. Xiong, Z.S. You, S.D. Qu, L. Lu
Fracture behavior of heterogeneous nanostructured 316L austenitic stainless steel with nanotwin bundles
Acta Mater., 150 (2018), pp. 130-138, 10.1016/j.actamat.2018.02.065
View PDFView articleView in ScopusGoogle Scholar
40. [40]
S.K. Putatunda
Fracture toughness of a high carbon and high silicon steel
Mater. Sci. Eng.: A, 297 (2001), pp. 31-43, 10.1016/s0921-5093(00)01272-7
View PDFView articleView in ScopusGoogle Scholar
41. [41]
B. Wang, Q.Q. Duan, P. Zhang, Z.J. Zhang, X.W. Li, Z.F. Zhang
Investigation on the cracking resistances of different ageing treated 18Ni maraging steels
Mater. Sci. Eng.: A, 771 (2020), Article 138553, 10.1016/j.msea.2019.138553
View PDFView articleView in ScopusGoogle Scholar
42. [42]
D.M. Jafarlou, C. Walde, V.K. Champagne, S. Krishnamurty, I.R. Grosse
Influence of cold sprayed Cr3C2-Ni coating on fracture characteristics of additively manufactured 15Cr-5Ni stainless steel

Mater. Des., 155 (2018), pp. 134-147, 10.1016/j.matdes.2018.05.063
View PDFView articleView in ScopusGoogle Scholar

43. [43]
V. Cain, L. Thijs, J. Van Humbeeck, B. Van Hooreweder, R. Knutsen
Crack propagation and fracture toughness of Ti6Al4V alloy produced by selective laser melting
Addit Manuf, 5 (2015), pp. 68-76, 10.1016/j.addma.2014.12.006
View PDFView articleView in ScopusGoogle Scholar

44. [44]
T.H. Becker, M. Beck, C. Scheffer
Microstructure and mechanical properties of direct metal laser sintered Ti-6Al-4V
South Afric. J. Ind. Eng., 26 (2015), pp. 1-10, 10.7166/26-1-1022
View in ScopusGoogle Scholar

45. [45]
D. Greitemeier, F. Palm, F. Syassen, T. Melz
Fatigue performance of additive manufactured TiAl6V4 using electron and laser beam melting
Int. J. Fatigue, 94 (2017), pp. 211-217, 10.1016/j.ijfatigue.2016.05.001
View PDFView articleView in ScopusGoogle Scholar

46. [46]
N. Kishore Babu, S. Ganesh Sundara Raman, R. Mythili, S. Saroja
Fracture toughness of Ti-6Al-4V after welding and postweld heat treatment
Weld J., 76 (1997), pp. 581-587, 10.1016/j.matchar.2006.07.001
Google Scholar

47. [47]
I. Sen, S. Tamirisakandala, D.B. Miracle, U. Ramamurty
Microstructural effects on the mechanical behavior of B-modified Ti–6Al–4V alloys
Acta Mater., 55 (2007), pp. 4983-4993, 10.1016/j.actamat.2007.05.009
View PDFView articleView in ScopusGoogle Scholar

48. [48]
A. Ranjan, J.S. Jha, S.K. Mishra
The role of microstructure inhomogeneity in Ti-6Al-4V forging on fracture toughness behavior
J. Mater. Eng. Perform., 31 (2022), pp. 7989-8003, 10.1007/s11665-022-06862-w
View in ScopusGoogle Scholar

49. [49]
A.W. Bowen
The influence of crystallographic orientation on the fracture toughness of strongly textured Ti-6Al-4V
Acta Metall., 26 (1978), pp. 1423-1433, 10.1016/0001-6160(78)90157-8
View PDFView articleView in ScopusGoogle Scholar

50. [50]
Z. Zhu, Z. Hu, H.L. Seet, T. Liu, W. Liao, U. Ramamurty, S.M. Ling Nai
Recent progress on the additive manufacturing of aluminum alloys and aluminum matrix composites: Microstructure, properties, and applications
Int. J. Mach. Tools Manuf, 190 (2023), Article 104047, 10.1016/j.ijmachtools.2023.104047
View PDFView articleView in ScopusGoogle Scholar

51. [51]

R. Casati, M. Vedani
Aging response of an A357 Al Alloy processed by selective laser melting
Adv. Eng. Mater., 21 (2019), Article 1800406, 10.1002/adem.201800406
View in ScopusGoogle Scholar
52. [52]
Y. Li, D. Gu
Parametric analysis of thermal behavior during selective laser melting additive manufacturing of aluminum alloy powder
Mater. Des., 63 (2014), pp. 856-867, 10.1016/j.matdes.2014.07.006
View PDFView articleView in ScopusGoogle Scholar
53. [53]
W.S. Miller, L. Zhuang, J. Bottema, A.J. Wittebrood, P. De Smet, A. Haszler, A. Vieregge
Recent development in aluminium alloys for the automotive industry
Mater. Sci. Eng. A, 280 (2000), pp. 37-49, 10.1016/s0921-5093(99)00653-x
View PDFView articleView in ScopusGoogle Scholar
54. [54]
D. Frómeta, S. Parareda, A. Lara, S. Molas, D. Casellas, P. Jonsén, J. Calvo
Identification of fracture toughness parameters to understand the fracture resistance of advanced high strength sheet steels
Eng. Fract. Mech., 229 (2020), Article 106949, 10.1016/j.engfracmech.2020.106949
View PDFView articleView in ScopusGoogle Scholar
55. [55]
D. Kong, C. Dong, S. Wei, X. Ni, L. Zhang, R. Li, L. Wang, C. Man, X. Li
About metastable cellular structure in additively manufactured austenitic stainless steels
Addit Manuf, 38 (2021), Article 101804, 10.1016/j.addma.2020.101804
View PDFView articleView in ScopusGoogle Scholar
56. [56]
L. Liu, Q. Ding, Y. Zhong, J. Zou, J. Wu, Y.L. Chiu, J. Li, Z. Zhang, Q. Yu, Z. Shen
Dislocation network in additive manufactured steel breaks strength–ductility trade-off
Mater. Today, 21 (2018), pp. 354-361, 10.1016/j.mattod.2017.11.004
View PDFView articleView in ScopusGoogle Scholar
57. [57]
L. Cui, S. Jiang, J. Xu, R.L. Peng, R.T. Mousavian, J. Moverare
Revealing relationships between microstructure and hardening nature of additively manufactured 316L stainless steel
Mater. Des., 198 (2021), Article 109385, 10.1016/j.matdes.2020.109385
View PDFView articleView in ScopusGoogle Scholar
58. [58]
T. Allam, K.G. Pradeep, P. Köhnen, A. Marshal, J.H. Schleifenbaum, C. Haase
Tailoring the nanostructure of laser powder bed fusion additively manufactured maraging steel
Addit. Manuf., 36 (2020), 10.1016/j.addma.2020.101561
Google Scholar
59. [59]
F.F. Conde, J.D. Escobar, J.P. Oliveira, M. Béreš, A.L. Jardini, W.W. Bose, J.A. Avila

Effect of thermal cycling and aging stages on the microstructure and bending strength of a selective laser melted 300-grade maraging steel
Mater. Sci. Eng. A, 758 (2019), pp. 192-201, 10.1016/j.msea.2019.03.129
View PDFView articleView in ScopusGoogle Scholar
60. [60]
B. Van Hooreweder, D. Moens, R. Boonen, J.P. Kruth, P. Sas
Analysis of fracture toughness and crack propagation of Ti6Al4V produced by selective laser melting
Adv. Eng. Mater., 14 (2012), pp. 92-97, 10.1002/adem.201100233
View in ScopusGoogle Scholar
61. [61]
S. Liu, Y.C. Shin
Additive manufacturing of Ti6Al4V alloy: a review
Mater. Des., 164 (2019), Article 107552, 10.1016/j.matdes.2018.107552
View PDFView articleView in ScopusGoogle Scholar
62. [62]
R.O. Ritchie, J.F. Knott, J.R. Rice
On the relationship between critical tensile stress and fracture toughness in mild steel
J. Mech. Phys. Solids, 21 (1973), pp. 395-410, 10.1016/0022-5096(73)90008-2
View PDFView articleView in ScopusGoogle Scholar
63. [63]
H.D. Nguyen, A. Pramanik, A.K. Basak, Y. Dong, C. Prakash, S. Debnath, S. Shankar, I.S. Jawahir, S. Dixit, D. Buddhi
A critical review on additive manufacturing of Ti-6Al-4V alloy: microstructure and mechanical properties
J. Mater. Res. Technol., 18 (2022), pp. 4641-4661, 10.1016/j.jmrt.2022.04.055
View PDFView articleView in ScopusGoogle Scholar
64. [64]
T.H. Becker, P. Kumar, U. Ramamurty
Fracture and fatigue in additively manufactured metals
Acta Mater., 219 (2021), Article 117240, 10.1016/j.actamat.2021.117240
View PDFView articleView in ScopusGoogle Scholar
65. [65]
B. Gludovatz, A. Hohenwarter, D. Catoor, E.H. Chang, E.P. George, R.O. Ritchie
A fracture-resistant high-entropy alloy for cryogenic applications
Science, 345 (2014), pp. 1153-1158, 10.1126/science.1254581
View in ScopusGoogle Scholar
66. [66]
B. Gludovatz, A. Hohenwarter, K.V.S. Thurston, H. Bei, Z. Wu, E.P. George, R.O. Ritchie
Exceptional damage-tolerance of a medium-entropy alloy CrCoNi at cryogenic temperatures
Nat. Commun., 7 (2016), pp. 1-8, 10.1038/ncomms10602
Google Scholar
67. [67]
D. Liu, Q. Yu, S. Kabra, M. Jiang, P. Forna-Kreutzer, R. Zhang, M. Payne, F. Walsh, B. Gludovatz, M. Asta, A.M. Minor, E.P. George, R.O. Ritchie

Exceptional fracture toughness of CrCoNi-based medium- and high-entropy alloys at 20 kelvin
Science, 378 (2022), pp. 978-983, 10.1126/science.abp8070
View in ScopusGoogle Scholar

68. [68]
D.H. Cook, P. Kumar, M.I. Payne, C.H. Belcher, P. Borges, W. Wang, F. Walsh, Z. Li, A. Devaraj, M. Zhang, M. Asta, A.M. Minor, E.J. Lavernia, D. Apelian, R.O. Ritchie
Kink bands promote exceptional fracture resistance in a NbTaTiHf refractory medium-entropy alloy
Science, 384 (2024), pp. 178-184, 10.1126/science.adn2428
View in ScopusGoogle Scholar

69. [69]
K. Li, W. Chen, G. Yu, J. Zhang, J. Sun
A novel deformation mechanism in Ti-V binary metastable β-Ti alloys: Deformation kinking promoted by dislocation accumulation
J. Alloys Compd., 875 (2021), Article 159982, 10.1016/j.jallcom.2021.159982
View PDFView articleView in ScopusGoogle Scholar

70. [70]
ASTM E8
ASTM E8/E8M Standard Test Methods for Tension Testing of Metallic Materials
Annual Book of ASTM Standards 4 ASTM Stds (2010), pp. 1-27, 10.1520/E0008-04
Google Scholar